# Characterization in Humans of $^{18}$F-MNI-444, a PET Radiotracer for Brain Adenosine 2A Receptors

Olivier Barret[1], Jonas Hannestad[2], Christine Vala[1], David Alagille[1], Adriana Tavares[1], Marc Laruelle[2], Danna Jennings[1], Ken Marek[1], David Russell[1], John Seibyl[1], and Gilles Tamagnan[1]

[1]*Molecular NeuroImaging, LLC, New Haven, Connecticut; and* [2]*UCB Pharma SPRL, Braine-l'Alleud, Belgium*

PET with selective adenosine 2A receptor ($A_{2A}$) radiotracers can be used to study a variety of neurodegenerative and neuropsychiatric disorders in vivo and to support drug-discovery studies targeting $A_{2A}$. The aim of this study was to describe the first in vivo evaluation of $^{18}$F-MNI-444, a novel PET radiotracer for imaging $A_{2A}$, in healthy human subjects. **Methods:** Ten healthy human volunteers were enrolled in this study; 6 completed the brain PET studies and 4 participated in the whole-body PET studies. Arterial blood was collected for invasive kinetic modeling of the brain PET data. Noninvasive methods of data quantification were also explored. Test–retest reproducibility was evaluated in 5 subjects. Radiotracer distribution and dosimetry was determined using serial whole-body PET images acquired over 6 h post-radiotracer injection. Urine samples were collected to calculate urinary excretion. **Results:** After intravenous bolus injection, $^{18}$F-MNI-444 rapidly entered the brain and displayed a distribution consistent with known $A_{2A}$ densities in the brain. Binding potentials ranging from 2.6 to 4.9 were measured in $A_{2A}$-rich regions, with an average test–retest variability of less than 10%. The estimated whole-body radiation effective dose was approximately 0.023 mSv/MBq. **Conclusion:** $^{18}$F-MNI-444 is a useful PET radiotracer for imaging $A_{2A}$ in the human brain. The superior in vivo brain kinetic properties of $^{18}$F-MNI-444, compared with previously developed $A_{2A}$ radiotracers, provide the opportunity to foster global use of in vivo $A_{2A}$ PET imaging in neuroscience research.

**Key Words:** $A_{2A}$ receptors; PET; $^{18}$F-MNI-444; kinetic modeling; dosimetry

**J Nucl Med 2015; 56:586–591**
DOI: 10.2967/jnumed.114.152546

The adenosine 2A receptor ($A_{2A}$) has attracted significant interest from the scientific community as a novel therapeutic target in Parkinson disease, mainly prompted by multiple studies demonstrating the coexpression of $A_{2A}$ and dopamine $D_2$ receptors in basal ganglia neurons (*1–4*). $A_{2A}$ has also been identified as a promising therapeutic target in Alzheimer disease, Huntington disease, mood disorders, panic disorder, schizophrenia, attention deficit hyperactivity disorder, and addiction (*5–9*).

PET and SPECT have the unique ability to assess neuroreceptors in vivo. The development of selective $A_{2A}$ radiotracers would provide the opportunity to study and understand multiple neuropsychiatric and neurodegenerative disorders and could also accelerate and aid drug-discovery programs targeting $A_{2A}$. In this context, several compounds have been proposed for in vivo imaging of $A_{2A}$ in the brain (*6,10–20*).

Until recently, all $A_{2A}$ radiotracers developed, either xanthine- or non–xanthine-derived radiotracers, have been labeled with the positron emitter $^{11}$C. Radiotracers labeled with longer-lived radioisotopes, such as $^{123}$I or $^{18}$F, which could be dispensed from a central radiopharmacy rather than generated on-site, would be advantageous, in particular in the conventional clinical setting in which no cyclotron facilities are typically available or in multicenter studies that require global distribution of radiotracers. In 2011, Bhattacharjee et al. developed $^{18}$F-MRS5425, and preliminary data in rodents demonstrated that striatal binding was blocked by preadministration of the selective $A_{2A}$ antagonist SCH442416 (*10*), but the potential utility of this radiotracer for imaging of $A_{2A}$ in the human brain remains untested. Recently, we reported on the development of the first, to our knowledge, successful iodinated $A_{2A}$ SPECT radiotracer, $^{123}$I-MNI-420, both in nonhuman and human primates (*16,17*). Subsequently, we developed an analog of MNI-420 labeled with $^{18}$F, $^{18}$F-MNI-444. Evaluation in nonhuman primates showed that this radiotracer held promise as an $A_{2A}$ PET radiotracer (*21*) with improved characteristics, compared with existing $A_{2A}$ tracers, and encouraged the validation of this imaging probe in humans. In this study, we report on the first in vivo evaluation of $^{18}$F-MNI-444 in healthy human volunteers. We describe the brain pharmacokinetic properties and test–retest results of $^{18}$F-MNI-444 as well as the whole-body biodistribution and dosimetry estimates of this $A_{2A}$ PET radiotracer.

## MATERIALS AND METHODS

### Radiochemistry

The radiolabeling and preparation of $^{18}$F-MNI-444 were described in detail previously (*21*). In brief, $^{18}$F-MNI-444 was prepared by reaction of the corresponding tosyl precursor, 2-(4-(4-(2-(5-amino-2-(furan-2-yl)-7H-pyrazolo[4,3-e][1,2,4]triazolo[1,5-c]pyrimidin-7-yl)ethyl)piperazin-1-yl)phenoxy)ethyl 4-methylbenzenesulfonate, with $^{18}F^-$ in anhydrous dimethylsulfoxide in the presence of potassium carbonate and Kryptofix 222 using a commercial synthesizer, TRACERlab FX-FN (GE Healthcare). The binding affinity for recombinant human $A_{2A}$ ($K_i$ = 2.8 nM) was measured using $^3$H-CGS21680 in transfected HEK-293 cells (assay performed by Cerep).

Quality control included visual inspection of appearance, pH, strength, pyrogen content, residual solvent, residual Kryptofix 222, radiochemical purity and identity, and specific activity (*21*). Identity and radiochemical purity were determined by high-performance liquid chromatography using a Phenomenex Kinetex-XB C18 (4.6 × 100 mm) column, eluted with methanol (solvent A) and 0.8% triethylamine in water (solvent B) with

Received Dec. 2, 2014; revision accepted Jan. 26, 2015.
For correspondence or reprints contact: Olivier Barret, Molecular NeuroImaging (MNI), LLC, 60 Temple St., Suite 8B, New Haven, CT 06510.
E-mail: obarret@mnimaging.com
Published online Feb. 19, 2015.

a linear gradient going from 50% A to 90% A in 12 min, maintained at 90% A until 15 min and returned to the initial condition at 15.1 min until the end of run at 20 min. The flow rate was 0.75 mL/min.

All productions showed a radiochemical purity above 99% and a specific activity exceeding 370 GBq/μmol. The average decay-corrected radiochemical yield was 24.5% ± 5.0% ($n$ = 39) in 60 min.

### Human Subjects

This study protocol was reviewed and approved by the New England Institutional Review Board. All subjects gave their written informed consent before participation in this study.

Ten healthy human volunteers (based on medical history and physical examination), 3 women and 7 men, with a mean age of 35.5 y (range, 22–52 y), were enrolled in this study. None of them had a known clinical history that could have affected the biodistribution or elimination of $^{18}$F-MNI-444. Six subjects (5 men and 1 woman; mean age ± SD, 38.1 ± 10.5 y; range, 23–52 y) completed $^{18}$F-MNI-444 brain PET studies. Four subjects, 2 men and 2 women (mean age ± SD, 28.3 ± 7.5 y; range, 22–39 y), participated in the whole-body imaging studies of $^{18}$F-MNI-444. All subjects were required to refrain from drinking caffeinated beverages for up to 12 h before the imaging session, given the known effect of caffeine on $A_{2A}$ (*16,17*).

### Brain PET Studies

PET images were acquired on an ECAT EXACT HR+ camera (Siemens) in 3 dimensions. Subjects were administered a single dose of $^{18}$F-MNI-444 (348.3 ± 59.6 MBq [9.41 ± 1.61 mCi]; range, 172.3–389.0 MBq [4.66–10.51 mCi]; 0.87 ± 0.35 μg [range, 0.35–1.51 μg]) as a slow intravenous injection over 3 min, followed by a 10-mL saline flush. Five of the 6 subjects underwent a second PET scan within 13–51 d of the first scan for test–retest variability assessment, for a total of 11 brain PET studies. Four subjects were imaged over 210 min (2 imaging sessions, 30-min break, first session of 90 min [3 scans] or 120 min [4 scans]) and 2 subjects were imaged over 120 min (1 imaging session, 4 scans), with frames from injection time of increasing duration from 30 s to 5 min. A transmission scan was obtained before each emission scan with an external $^{68}$Ge rod source. PET data were corrected for randoms, dead time, scatter, and attenuation, and PET images were reconstructed using an ordered-subset expectation maximization algorithm (4 iterations, 16 subsets, post gaussian filter with kernel of 5 mm).

A structural 3-dimensional T1-weighted MR image was acquired for all subjects on an Espree 1.5-T scanner (Siemens) (magnetization-prepared rapid acquisition with gradient echo; inversion time, 1.1 s; repetition time, 1.97 s; echo time, 3.17 ms; flip angle, 15°).

In the 5 subjects who underwent 2 PET scans, arterial blood samples were collected from the ulnar or radial arteries every 45 s until 6 min after injection and at 8, 10, 15, 20, 25, 30, 45, 60, 90, and 120 min and then at 150, 180, and 210 min for brain PET studies with 2 imaging sessions. Radioactivity in whole blood and plasma was measured for all samples in a well-type γ counter (Wallac 2480; Perkin Elmer). A subset of samples (6, 15, 30, 60, and 90 and 120, 150, and 210 min) was processed to estimate the fraction of intact $^{18}$F-MNI-444 by acetonitrile denaturation and analyzed by reversed-phase high-performance liquid chromatography on a Phenomenex Luna C18(2) (10 × 250 mm, 10 μm) column with a mobile phase consisting of a mixture of methanol/water with 0.8% of triethylamine in a 70/30 ratio at a flow rate of 4.0 mL/min. The plasma free-fraction ($f$p) was evaluated using a preinjection blood sample spiked at the time of processing with approximately 15 kBq/mL of $^{18}$F-MNI-444. Aliquots of plasma (200 μL) were placed in ultrafiltration units (Amicon Centrifree 30K; Millipore) and centrifuged at 20° C for 20 min at 3,000$g$. The $f$p was calculated as the ratio of the ultrafiltrate to the plasma activity (*21*).

Images were analyzed in PMOD 3.405 software (PMOD Technologies). Images were corrected for motion within each imaging session.

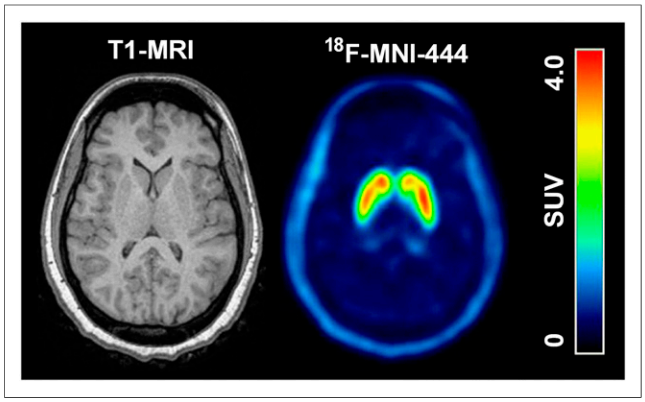


**FIGURE 1.** Representative transverse PET sum image (30–90 min) of $^{18}$F-MNI-444 distribution in human brain with correspondent T1 MR image.

PET images were cross-calibrated with the well counter used for blood measurements, and when 2 imaging sessions were acquired, both PET series were merged and corrected for decay. Initial flowlike PET images (~15 min) were averaged and used to align the whole PET series onto the subject T1-weighted structural MR image, and subsequently both

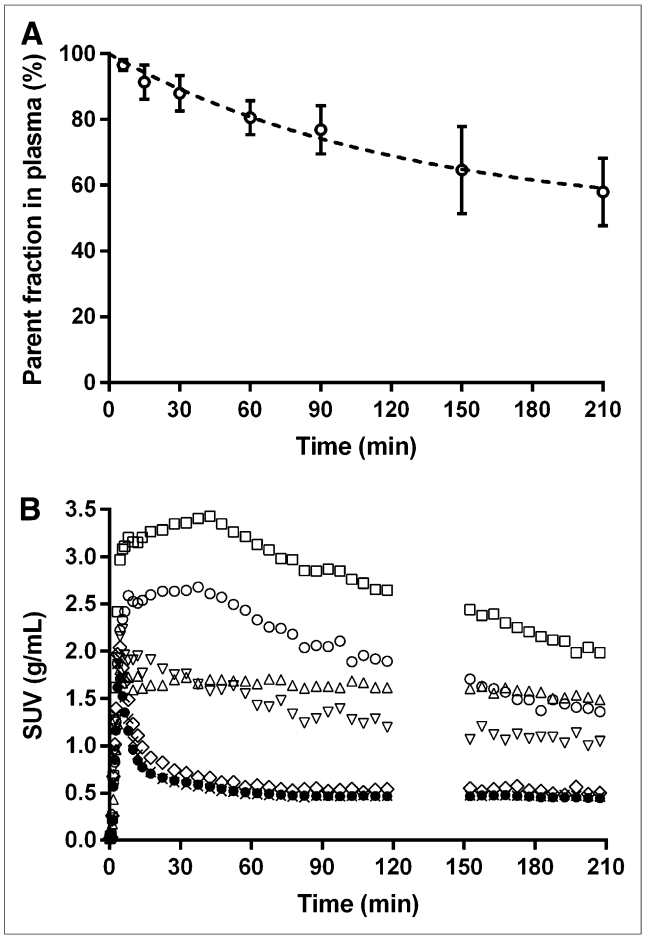


**FIGURE 2.** (A) Parent fraction profile in arterial plasma after intravenous administration of $^{18}$F-MNI-444 (mean ± SD, $n$ = 10 up to 90 min, $n$ = 6 afterward). (B) Representative $^{18}$F-MNI-444 time–activity curves in a healthy human subject over 3.5 h. ○ = caudate; □ = putamen; △ = globus pallidus; ▽ = nucleus accumbens; ◇ = thalamus; ● = frontal cortex; × = cerebellum.

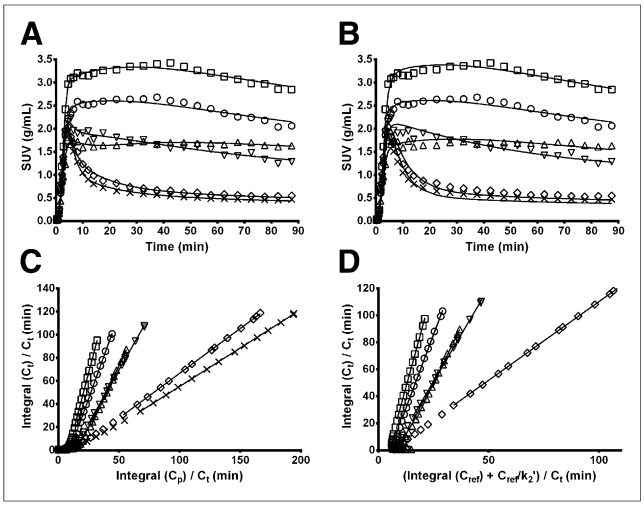


**FIGURE 3.** $^{18}$F-MNI-444 time–activity curves over 90 min showing in solid line 2TCM fits (A); 1TCM fits (B); Logan graphical analysis plots, linear regression ($t^*$ = 20 min) (C); and noninvasive Logan graphical analysis, linear regression ($t^*$ = 20 min and $k_2'$ = 0.15 min$^{-1}$) (D). ○ = caudate; □ = putamen; △ = globus pallidus; ▽ = nucleus accumbens; ◇ = thalamus; × = cerebellum.

MR imaging and PET series were spatially normalized to the standard Montreal Neurologic Institute space. The probabilistic volume of interest (VOI) atlas by Hammers et al. (*22*) was applied to normalized $^{18}$F-MNI-444 PET images, and time–activity curves were extracted for the following brain regions: caudate, putamen, globus pallidus, nucleus accumbens, thalamus, frontal cortex, parietal cortex, temporal cortex, occipital cortex, and cerebellum. Standardized uptake values (SUVs) were calculated by normalizing the uptake values by the injected dose (ID) divided by the subject weight.

Kinetic modeling was performed using compartmental analysis with standard 1-tissue models (1TCM) and 2-tissue models (2TCM) and Logan graphical analysis (LGA) with $t^*$ = 20 min using the radiometabolite-corrected arterial plasma input function to estimate the volume of distribution ($V_T$) in different brain regions (*23,24*). The binding potential $BP_{ND}$ was calculated indirectly as $(V_T - V_{ND})/V_{ND}$, where $V_{ND}$ was the $V_T$ of the reference region (*23*). In addition, $BP_{ND}$ was also estimated using the noninvasive LGA (NI-LGA) (*25*) with $t^*$ = 20 min and $k_2'$ = 0.15 min$^{-1}$, as well as from the SUVr (SUV ratio to the reference region) between 60 and 90 min after radiotracer injection as $BP_{ND}$ = SUVr-1. The cerebellum, shown to have low to negligible $A_{2A}$ density in autoradiography experiments (*26,27*) and previously used in studies with $A_{2A}$ radiotracers (*13,14,21*), was used as the reference region for data quantification. Finally, the test–retest reproducibility for $V_T$ and $BP_{ND}$ was estimated as ABS(test − retest)/AVERAGE(test + retest) (where ABS is absolute value).

### Whole-Body PET Studies

Whole-body PET images were acquired on an ECAT EXACT HR+ camera. Healthy controls (2 men, 2 women) received a bolus intravenous administration of $^{18}$F-MNI-444 (360.8 ± 7.1 MBq [9.75 ± 0.19 mCi]; range, 351.3–367.3 MBq [9.50–9.93 mCi]; 0.83 ± 0.39 μg [range, 0.33–1.17 μg]), and immediately following a series of whole-body 2D PET images consisting of 9 contiguous bed positions was obtained. Images were acquired over approximately 360 min in 3 scanning sessions, with subjects being allowed out of the camera for 20 min between sessions. The first session included 5 whole-body passes (2 × 60 s and 3 × 120 s per bed position), and the last 2 sessions included 2 whole-body passes each (2 × 270 s per bed position). A transmission scan was acquired before each imaging session with an external $^{68}$Ge rod source. PET data were corrected for photon attenuation, scatter, and random and reconstructed using ordered-subset expectation maximization (4 iterations, 16 subsets) with no filtering.

Urine was collected for up to 6 h after radiotracer injection to measure the fraction of activity voided by the renal system. Activity not excreted in urine was assumed to be eliminated in feces.

For each subject, VOIs were drawn around organs that displayed higher radioactivity concentration than background—that is, source organs. The delineated VOIs were applied to all acquired frames and, if needed, adjusted for subject position at different acquisition sessions, while keeping their shapes and sizes constant. The following organs were identified as source organs: brain, heart, liver, gallbladder, intestine, kidneys, urinary bladder, and spleen. A whole-body VOI was drawn around the subject's body and used for quantification of whole-body remainder activity as whole-body activity minus source organ activity.

Non–decay-corrected time–activity curves were generated for each source organ, expressed as percentage ID (%ID). After the last measured time point, elimination was assumed to be through physical decay only. The residence time τ, defined as the ratio of accumulated activity in the source organ ($\tilde{A}$) and injected activity ($A_0$), $\tau = \tilde{A}/A_0$, was calculated as the area under the curve of the tissue time–activity curve from time zero to infinity using the trapezoidal method. Radiation absorbed dose and effective dose (weighted average using ICRP 60 tissue-weighting factors (*28*)) were estimated with the OLINDA/EXM 1.0 software package (*29*) using the calculated τ. Intestinal τ values were estimated using the ICRP 30 gastrointestinal model (*30*) as incorporated in OLINDA; the intestinal decay-corrected time–activity curve was used for estimation of the highest fraction of activity entering the intestine. The adult male and female models, adjusted to each individual body mass, were assumed for the male and female subjects, respectively.

## RESULTS

### Brain Studies

After intravenous bolus injection, $^{18}$F-MNI-444 rapidly entered the human brain. The radiotracer accumulation was highest in the caudate and putamen, regions known to contain high densities of $A_{2A}$, and low in cortical areas and cerebellum (Figs. 1 and 2B), with peak uptake in the putamen of 3.0–4.0 SUV around 30 min after injection and much faster washout in the cerebellum (peak uptake within 5 min of injection).

A slow metabolism of the parent radiotracer was observed (Fig. 2A). At 90 and 210 min after radiotracer injection, the parent fraction

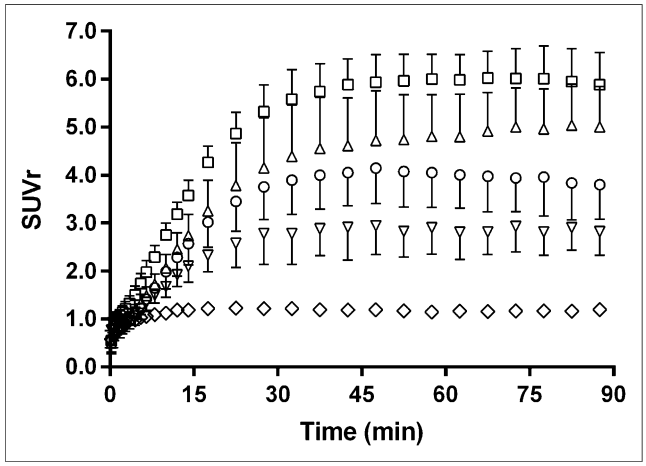


**FIGURE 4.** SUVr curves (mean ± SD, $n$ = 11), showing relatively stable values from 45 min after $^{18}$F-MNI-444 injection. ○ = caudate; □ = putamen; △ = globus pallidus; ▽ = nucleus accumbens; ◇ = thalamus.

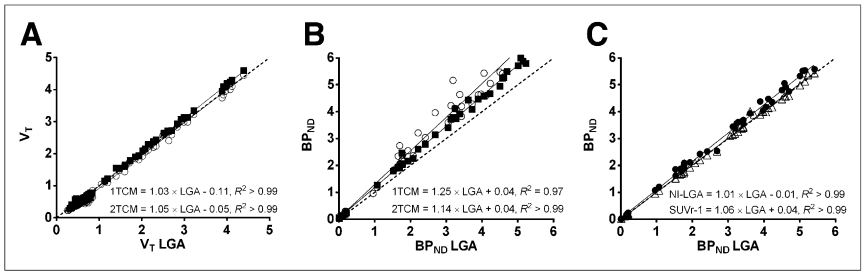


**FIGURE 5.** (A) Correlation of LGA $V_T$ (all regions) against 1TCM and 2TCM estimates. Correlation of LGA $BP_{ND}$ (caudate, putamen, globus pallidus, nucleus accumbens, and thalamus) against 1TCM and 2TCM (B) or NI-LGA and SUVr-1 (60–90 min) (C) estimates. All estimates obtained by modeling 90 min of imaging data. ○ = 1TCM; ■ = 2TCM; △ = NI-LGA; ● = SUVr-1; solid line = linear regression; dashed line = line of identity.

in arterial plasma was 78.1% ± 9.2% ($n$ = 10) and 61.5% ± 6.6% ($n$ = 6), respectively.

Typical 2TCM and 1TCM fits and LGA and NI-LGA plots are provided in Figure 3. 2TCM provided better fits than 1TCM based on the Akaike information and model selection criteria, in particular in the low-uptake regions, but had convergence issues in high-uptake regions for 1 subject. The average SUVr graph is also given in Figure 4, showing that pseudoequilibrium of the tissue ratios was attained from about 45 min after injection.

Correlations of $V_T$ and $BP_{ND}$ obtained with 2TCM, 1TCM, LGA, and NI-LGA are provided in Figure 5. 2TCM and 1TCM $V_T$ correlated well with LGA, close to the line of identity, with an $R^2$ greater than 0.99 (Fig. 5A), but 2TCM and 1TCM overestimated $BP_{ND}$, compared with LGA (Fig. 5B), due to the lower $V_T$ estimated in the cerebellum with 2TCM and 1TCM (negative $y$-intercept in Fig. 5A). There is, however, good agreement between LGA $BP_{ND}$ and NI-LGA and a small overestimation of SUVr-1 of 6% (Fig. 5C).

Results for $V_T$ and $BP_{ND}$ obtained with the LGA, NI-LGA, and SUVr methods are summarized in Table 1, with the highest $V_T$ and $BP_{ND}$ values measured in the putamen, globus pallidus, caudate, and nucleus accumbens, $A_{2A}$-rich regions (cortical area $V_T$ close to that in the cerebellum [Fig. 2B for the frontal cortex]), with a $BP_{ND}$ close to 5.0 in the putamen. The impact of the acquisition duration was also investigated, and when the whole dataset (210 min of data) was used, $V_T$ increased by 3% and $BP_{ND}$ decreased by 9%.

The average $V_T$ and $BP_{ND}$ estimates in the test and retest studies are shown in Figure 6. The LGA $V_T$ test–retest variability in the caudate, putamen, globus pallidus, nucleus accumbens, and cerebellum was estimated as 12.7%, 10.1%, 10.4%, 6.8%, 12.0%, and 10.0%, respectively. For $BP_{ND}$, the variability in the caudate, putamen, globus pallidus, and nucleus accumbens was 9.7%, 5.2%, 8.3%, and 10.2% for LGA; 10.8%, 6.2%, 8.8%, and 10.0% for NI-LGA; and 11.4%, 6.6%, 5.3%, and 9.3% for the SUVr method, respectively, but higher in the thalamus (~23% for LGA and NI-LGA and ~50% for the SUVr method) given the low $BP_{ND}$ in that region (~0.2).

### Whole-Body PET Studies

$^{18}$F-MNI-444 whole-body distribution over time is provided in Supplemental Fig. 1 (supplemental materials are available at http://jnm.snmjournals.org), demonstrating early distribution in the blood pool and elimination of the radioactivity mainly via the hepatobiliary system, with the radioactivity present in the urine over a 6-h period measured to be less than 7% of the injected dose. The τ values were highest for the liver and intestine, with a peak %ID in the liver of 29.0% ± 3.9% at 16 min after radiotracer injection. Peak %ID in other organs were much lower, with 7.3% ± 1.3% in the intestine, 3.4% ± 0.8% in the brain, and 2.4% ± 0.2% in the heart and all other organs below 1.0%.

Table 2 lists the average absorbed doses and the effective dose for $^{18}$F-MNI-444. The mean effective dose for a human subject was found to be 0.023 ± 0.001 mSv/MBq, with the upper large intestinal wall receiving the highest absorbed dose of approximately 0.099 mSv/MBq.

## DISCUSSION

In this article, we reported the first, to our knowledge, in vivo human PET study conducted to evaluate $^{18}$F-MNI-444 pharmacokinetic properties in the brain and dosimetry estimates in healthy human volunteers. $^{18}$F-MNI-444 distribution in the brain was consistent with known $A_{2A}$ densities from autoradiography reports (*26,27*) and with our prior observations in the nonhuman primate brain (*21*). The distribution volumes estimated with the Logan graphical analysis showed a good correlation with the 1TCM and 2TCM estimates, and given the fitting issues of 1TCM in low-uptake regions and the convergence issues of 2TCM in high-uptake regions, the graphical analysis was taken as the preferred method

**TABLE 1**
$^{18}$F-MNI-444 $V_T$, $BP_{ND}$, and SUVr Estimates

| Brain region | LGA $V_T$ | LGA $BP_{ND}$ | NI-LGA $BP_{ND}$ | SUVr-1 |
|---|---|---|---|---|
| Caudate | 2.10 ± 0.69 | 2.69 ± 0.74 | 2.81 ± 0.80 | 2.93 ± 0.72 |
| Putamen | 3.26 ± 0.98 | 4.70 ± 0.63 | 4.80 ± 0.69 | 5.00 ± 0.61 |
| Globus pallidus | 2.64 ± 0.83 | 3.67 ± 0.69 | 3.86 ± 0.90 | 3.96 ± 0.81 |
| Nucleus accumbens | 1.49 ± 0.48 | 1.60 ± 0.34 | 1.79 ± 0.73 | 1.86 ± 0.47 |
| Thalamus | 0.65 ± 0.17 | 0.15 ± 0.07 | 0.25 ± 0.34 | 0.17 ± 0.09 |
| Cerebellum | 0.57 ± 0.17 | NA | NA | NA |

Results obtained by modeling 90 min of imaging data and presented as mean ± SD ($n$ = 10). SUVr determined as average between 60 and 90 min after radiotracer injection.
NA = not applicable.

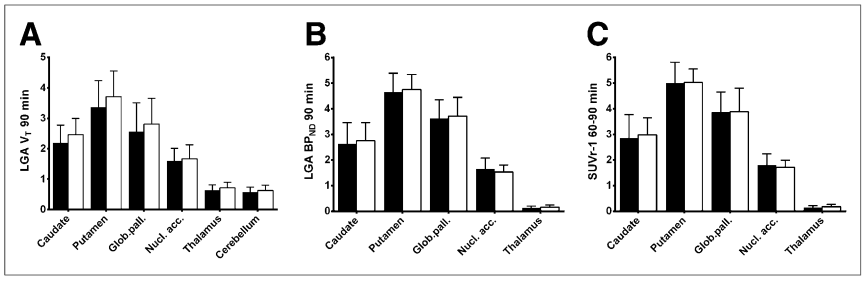


**FIGURE 6.** Bar graphs of average estimates ($n$ = 5, error bars = SD) obtained during test (black) and retest (white) studies for LGA $V_T$ (A), LGA $BP_{ND}$ (B), and SUVr-1 60–90 min (C).

for the analysis of $^{18}$F-MNI-444 dynamic PET data. Data collected in this study showed that $^{18}$F-MNI-444 displayed high $BP_{ND}$ values in $A_{2A}$-rich regions, up to 5.0 in the putamen.

The target-to-nontarget ratios and $BP_{ND}$s measured in this study were expressively higher than those reported by other researchers using $^{11}$C-SCH442416 and [7-methyl-$^{11}$C]-(*E*)-8-(3,4,5-trimethoxystyryl)-1,3,7-trimethylxanthine ($^{11}$C-TMSX), the other 2 PET radiotracers currently in human use. For example, the highest $BP_{ND}$ values reported in human caudate and putamen for $^{11}$C-SCH442416 and $^{11}$C-TMSX were around 0.5–1.0 and 1.0–1.5, respectively (*15,31,32*). $^{18}$F-MNI-444 also compares favorably with the iodinated SPECT analog $^{123}$I-MNI-420, for which we have previously reported striatal $BP_{ND}$ values that ranged between 0.8 and 1.2 in the human brain (*17*).

In this in vivo evaluation of $^{18}$F-MNI-444 in humans, we scanned human subjects over a period of up to approximately 3.5 h after radiotracer injection. Performing kinetic modeling using the full length of the PET series or truncating to 90 min of data marginally underestimated $V_T$ by about 3% and overestimated $BP_{ND}$ by about 9%. Moreover, a good $BP_{ND}$ test–retest reproducibility was obtained for 90 min of PET data (on average $<$ 10%). Taken together, the data suggested that quantification of $A_{2A}$ in the brain using $^{18}$F-MNI-444 could be successfully achieved by acquiring only 90 min of data.

Noninvasive methods of analysis were found to be suitable for quantification of $^{18}$F-MNI-444 brain PET data, for which we found a good correlation between invasive and noninvasive methods of quantification ($R^2 > 0.99$) and a small (~6% for SUVr) bias for $BP_{ND}$ estimates. The cerebellum was used as a reference region for estimation of tissue ratios and $BP_{ND}$s, given the low uptake observed in this region and previously published data indicating the low to negligible $A_{2A}$ density in the cerebellum in different species (*26,27*). Previously, we have observed that this region was suitable for quantification of $^{123}$I-MNI-420 SPECT images. High doses of caffeine or the selective $A_{2A}$ antagonist preladenant did not reduce $^{123}$I-MNI-420 cerebellar uptake in monkeys (*16*), and this was confirmed with $^{18}$F-MNI-444 against preladenant or tozadenant, another selective $A_{2A}$ antagonist (*21*).

The search for simplified methods of analysis often requires a trade-off between accuracy and simplicity. Given the good agreement between $V_T$ and $BP_{ND}$ values determined using longer and shorter acquisitions, as well as between noninvasive and invasive methods of quantification ($R^2 > 0.99$), and the small bias associated with these simplifications, the shortening of the PET acquisition or the acquisition of data between 60 and 90 min after radiotracer injection and the use of the cerebellum for data quantification seem to be suitable approaches for evaluation of $A_{2A}$ in the brain using PET with $^{18}$F-MNI-444. The use of simple ratios methods (SUVr between 60 and 90 min) will, however, have to be confirmed in human subjects with blocking studies with a selective $A_{2A}$ antagonist and in patient populations.

Whole-body PET imaging studies after intravenous injection of $^{18}$F-MNI-444 in healthy human volunteers showed that this radiotracer's main elimination route was hepatobiliary. The determined mean effective dose of approximately 0.023 mSv/MBq suggests only modest radiation exposure associated with $^{18}$F-MNI-444 imaging in humans and allows for multiple scans to be acquired in the same research subject per year. Furthermore, the determined effective dose is similar to that of other $^{18}$F-labeled radiotracers currently used in human studies. For example, the whole-body effective dose determined after intravenous injection of $^{18}$F-FDG was found to be around 0.029 mSv/MBq (*33*).

**TABLE 2**
$^{18}$F-MNI-444 Radiation Absorbed and Effective Doses (mSv/MBq)

| Organ | Mean | SD |
|---|---|---|
| Adrenals | 1.76E−02 | 2.86E−03 |
| Brain | 7.24E−03 | 1.19E−03 |
| Breasts | 8.86E−03 | 1.27E−03 |
| Gallbladder wall | 6.39E−02 | 9.26E−03 |
| Lower large intestinal wall | 3.74E−02 | 5.62E−03 |
| Small intestine | 8.87E−02 | 1.59E−02 |
| Stomach wall | 1.62E−02 | 1.32E−03 |
| Upper large intestinal wall | 9.87E−02 | 1.93E−02 |
| Heart wall | 1.79E−02 | 2.05E−03 |
| Kidneys | 2.29E−02 | 1.88E−03 |
| Liver | 7.86E−02 | 2.61E−02 |
| Lungs | 1.23E−02 | 2.20E−03 |
| Muscle | 1.16E−02 | 1.08E−03 |
| Ovaries | 2.41E−02 | 1.73E−03 |
| Pancreas | 1.86E−02 | 2.21E−03 |
| Red marrow | 1.23E−02 | 7.63E−04 |
| Osteogenic cells | 1.61E−02 | 2.13E−03 |
| Skin | 8.14E−03 | 8.85E−04 |
| Spleen | 2.53E−02 | 7.28E−03 |
| Testes | 8.76E−03 | 3.68E−04 |
| Thymus | 1.05E−02 | 1.47E−03 |
| Thyroid | 9.03E−03 | 7.74E−04 |
| Urinary bladder | 2.73E−02 | 9.35E−03 |
| Uterus | 2.11E−02 | 1.17E−03 |
| Total body | 1.45E−02 | 1.39E−03 |
| Effective dose (ICRP 60 (*28*)) | 2.31E−02 | 9.29E−04 |

## CONCLUSION

Data reported here demonstrated that $^{18}$F-MNI-444 is a useful PET radiotracer for in vivo imaging of $A_{2A}$ in the human brain. Kinetic modeling results indicated that the cerebellum can be used

as a reference region for data analysis with 90-min PET imaging. The estimated mean effective dose suggests that an acceptably low radiation exposure is associated with $^{18}$F-MNI-444 imaging in human subjects, and it is consistent with values reported for other PET radiotracers currently in human use. The development of $^{18}$F-MNI-444 provides the opportunity to further expand the global use of in vivo $A_{2A}$ PET imaging in neuroscience research.

## DISCLOSURE

The costs of publication of this article were defrayed in part by the payment of page charges. Therefore, and solely to indicate this fact, this article is hereby marked "advertisement" in accordance with 18 USC section 1734. No potential conflict of interest relevant to this article was reported.

## REFERENCES

1. Fuxe K, Agnati LF, Jacobsen K, et al. Receptor heteromerization in adenosine A2A receptor signaling: relevance for striatal function and Parkinson's disease. *Neurology.* 2003;61:S19–S23.
2. Ferré S, Ciruela F, Quiroz C, et al. Adenosine receptor heteromers and their integrative role in striatal function. *Scientific World Journal.* 2007;7:74–85.
3. Ferré S, Quiroz C, Woods AS, et al. An update on adenosine A2A-dopamine D2 receptor interactions: implications for the function of G protein-coupled receptors. *Curr Pharm Des.* 2008;14:1468–1474.
4. Ikeda K, Kurokawa M, Aoyama S, Kuwana Y. Neuroprotection by adenosine A2A receptor blockade in experimental models of Parkinson's disease. *J Neurochem.* 2002;80:262–270.
5. Muller CE, Jacobson KA. Recent developments in adenosine receptor ligands and their potential as novel drugs. *Biochim Biophys Acta.* 2011;1808:1290–1308.
6. Holschbach MH, Bier D, Stusgen S, et al. Synthesis and evaluation of 7-amino-2-(2(3)-furyl)-5-phenylethylamino-oxazolo[5,4-d]pyrimidines as potential A2A adenosine receptor antagonists for positron emission tomography (PET). *Eur J Med Chem.* 2006;41:7–15.
7. Chen JF, Eltzschig HK, Fredholm BB. Adenosine receptors as drug targets: what are the challenges? *Nat Rev Drug Discov.* 2013;12:265–286.
8. Ledent C, Vaugeois J-M, Schiffmann SN, et al. Aggressiveness, hypoalgesia and high blood pressure in mice lacking the adenosine $A_{2a}$ receptor. *Nature.* 1997;388:674–678.
9. El Yacoubi M, Ledent C, Parmentier M, et al. Adenosine A2A receptor antagonists are potential antidepressants: evidence based on pharmacology and A2A receptor knockout mice. *Br J Pharmacol.* 2001;134:68–77.
10. Bhattacharjee AK, Lang L, Jacobson O, et al. Striatal adenosine $A_{2A}$ receptor-mediated positron emission tomographic imaging in 6-hydroxydopamine-lesioned rats using [$^{18}$F]-MRS5425. *Nucl Med Biol.* 2011;38:897–906.
11. Hirani E, Gillies J, Karasawa A, et al. Evaluation of [4-*O-methyl*-$^{11}$C]KW-6002 as a potential PET ligand for mapping central adenosine $A_{2A}$ receptors in rats. *Synapse.* 2001;42:164–176.
12. Ishiwata K, Mishina M, Kimura Y, Oda K, Sasaki T, Ishii K. First visualization of adenosine $A_{2A}$ receptors in the human brain by positron emission tomography with [$^{11}$C]TMSX. *Synapse.* 2005;55:133–136.
13. Ishiwata K, Noguchi J, Wakabayashi S, et al. $^{11}$C-labeled KF18446: a potential central nervous system adenosine A2a receptor ligand. *J Nucl Med.* 2000;41:345–354.
14. Moresco RM, Todde S, Belloli S, et al. In vivo imaging of adenosine A2A receptors in rat and primate brain using [$^{11}$C]SCH442416. *Eur J Nucl Med Mol Imaging.* 2005;32:405–413.
15. Naganawa M, Kimura Y, Mishina M, et al. Quantification of adenosine A2A receptors in the human brain using [$^{11}$C]TMSX and positron emission tomography. *Eur J Nucl Med Mol Imaging.* 2007;34:679–687.
16. Tavares AA, Batis J, Barret O, et al. In vivo evaluation of [$^{123}$I]MNI-420: a novel single photon emission computed tomography radiotracer for imaging of adenosine 2A receptors in brain. *Nucl Med Biol.* 2013;40:403–409.
17. Tavares AA, Batis JC, Papin C, et al. Kinetic modeling, test-retest, and dosimetry of $^{123}$I-MNI-420 in humans. *J Nucl Med.* 2013;54:1760–1767.
18. Wells L, Salinas C, Tang SP, et al. Evaluation of the adenosine A2A receptor ligand [$^{11}$C] SCH442416 in the rodent brain [abstract]. *J Nucl Med.* 2013;54 (suppl 2):382.
19. Noguchi J, Ishiwata K, Wakabayashi S, et al. Evaluation of carbon-11-labeled KF17837: a potential CNS adenosine A2a receptor ligand. *J Nucl Med.* 1998;39:498–503.
20. Stone-Elander S, Thorell JO, Eriksson L, Fredholm BB, Ingvar M. In vivo biodistribution of [N-$^{11}$C-methyl]KF 17837 using 3-D-PET: evaluation as a ligand for the study of adenosine A2A receptors. *Nucl Med Biol.* 1997;24:187–191.
21. Barret O, Hannestad J, Alagille D, et al. Adenosine 2A receptor occupancy by tozadenant and preladenant in rhesus monkeys. *J Nucl Med.* 2014;55:1712–1718.
22. Hammers A, Allom R, Koepp MJ, et al. Three-dimensional maximum probability atlas of the human brain, with particular reference to the temporal lobe. *Hum Brain Mapp.* 2003;19:224–247.
23. Innis RB, Cunningham VJ, Delforge J, et al. Consensus nomenclature for in vivo :imaging of reversibly binding radioligands. *J Cereb Blood Flow Metab.* 2007;27: 1533–1539.
24. Logan J. Graphical analysis of PET data applied to reversible and irreversible tracers. *Nucl Med Biol.* 2000;27:661–670.
25. Logan J, Fowler JS, Volkow ND, Wang GJ, Ding YS, Alexoff DL. Distribution volume ratios without blood sampling from graphical analysis of PET data. *J Cereb Blood Flow Metab.* 1996;16:834–840.
26. Sihver W, Schulze A, Wutz W, et al. Autoradiographic comparison of in vitro binding characteristics of various tritiated adenosine A2A receptor ligands in rat, mouse and pig brain and first ex vivo results. *Eur J Pharmacol.* 2009;616:107–114.
27. Svenningsson P, Hall H, Sedvall G, Fredholm BB. Distribution of adenosine receptors in the postmortem human brain: an extended autoradiographic study. *Synapse.* 1997;27:322–335.
28. International Commission on Radiological Protection (ICRP). *1990 Recommendations of the International Commission on Radiological Protection.* ICRP publication 60. New York, NY: Pergamon Press; 1991.
29. Stabin MG, Sparks RB, Crowe E. OLINDA/EXM: the second-generation personal computer software for internal dose assessment in nuclear medicine. *J Nucl Med.* 2005;46:1023–1027.
30. International Commission on Radiological Protection (ICRP). *Limits for Intakes of Radionuclides by Workers.* ICRP publication 30 (part 1). Oxford, U.K.: ICRP; 1979.
31. Ramlackhansingh AF, Bose SK, Ahmed I, Turkheimer FE, Pavese N, Brooks DJ. Adenosine 2A receptor availability in dyskinetic and nondyskinetic patients with Parkinson disease. *Neurology.* 2011;76:1811–1816.
32. Mishina M, Ishiwata K, Naganawa M, et al. Adenosine $A_{2A}$ receptors measured with [C]TMSX PET in the striata of Parkinson's disease patients. *PLoS ONE.* 2011;6:e17338.
33. Deloar HM, Fujiwara T, Shidahara M, et al. Estimation of absorbed dose for 2-[F-18]fluoro-2-deoxy-D-glucose using whole-body positron emission tomography and magnetic resonance imaging. *Eur J Nucl Med.* 1998;25:565–574.

JNM The Journal of NUCLEAR MEDICINE

# Characterization in Humans of $^{18}$F-MNI-444, a PET Radiotracer for Brain Adenosine 2A Receptors

Olivier Barret, Jonas Hannestad, Christine Vala, David Alagille, Adriana Tavares, Marc Laruelle, Danna Jennings, Ken Marek, David Russell, John Seibyl and Gilles Tamagnan

*J Nucl Med.* 2015;56:586-591.
Published online: February 19, 2015.
Doi: 10.2967/jnumed.114.152546



*The Journal of Nuclear Medicine* is published monthly.
SNMMI | Society of Nuclear Medicine and Molecular Imaging
1850 Samuel Morse Drive, Reston, VA 20190.
(Print ISSN: 0161-5505, Online ISSN: 2159-662X)



SNMMI SOCIETY OF NUCLEAR MEDICINE AND MOLECULAR IMAGING